Quantifying the spatial, temporal, angular and spectral structure of effective daylight in perceptually meaningful ways

Yu, Cehao; Wijntjes, Maarten; Eisemann, Elmar; Pont, Sylvia

DOI
10.1364/OE.479715

Publication date
2023

Document Version
Final published version

Published in
Optics Express

Citation (APA)
Yu, C., Wijntjes, M., Eisemann, E., & Pont, S. (2023). Quantifying the spatial, temporal, angular and spectral structure of effective daylight in perceptually meaningful ways. *Optics Express*, *31*(5), 8953-8974. https://doi.org/10.1364/OE.479715

Research Article Vol. 31, No. 5 / 27 Feb 2023 / Optics Express 8953
Optics EXPRESS

Quantifying the spatial, temporal, angular and spectral structure of effective daylight in perceptually meaningful ways

CEHAO YU,[1,*] MAARTEN WIJNTJES,[1] ELMAR EISEMANN,[2] AND SYLVIA PONT[1]

[1] *Perceptual Intelligence Lab (π-Lab), Faculty of Industrial Design Engineering, Delft University of Technology, Delft, The Netherlands*
[2] *Computer Graphics and Visualization Group, Faculty of Electrical Engineering, Mathematics and Computer Science, Delft University of Technology, Delft, The Netherlands*
[*] *c.yu-2@tudelft.nl*

10.1364/opticaopen.21922866

Abstract: We present a method to capture the 7-dimensional light field structure, and translate it into perceptually-relevant information. Our spectral cubic illumination method quantifies objective correlates of perceptually relevant diffuse and directed light components, including their variations over time, space, in color and direction, and the environment's response to sky and sunlight. We applied it "in the wild", capturing how light on a sunny day differs between light and shadow, and how light varies over sunny and cloudy days. We discuss the added value of our method for capturing nuanced lighting effects on scene and object appearance, such as chromatic gradients.

1. Introduction

Measurements of the light environment play a crucial role in diverse fields such as architecture, lighting design, vision science and visual ergonomics. They need to characterize light in a human perception-based manner to provide meaningful information for human-centred fields and applications. In this context, photometry [1] instead of radiometry is required. Natural light varies as a function of space, direction, wavelength and time. In this paper, we focus on the question how to capture and describe perceptually meaningful light qualities relating to the complexity of all those variations in an effective manner.

Gershun first introduced the concept of the light field as a way to formally describe how light is structured in a three-dimensional scene [2]. He coined the light field as a function of radiance depending on location (x,y,z), direction (θ, φ), wavelength (λ) and time (t). This function is thus seven-dimensional, and in human vision it is known as the plenoptic function [3], which quantifies all optic information that is potentially available to an observer. In that sense it provides a starting point for studying objective aspects of the light environment. The visual light field describes the observers' subjective inferences of the physical light field, which generally differ from the objective physical ones [4–6]. Here we focus on the physical light field. However, in order to derive information from the light-field measurements that are meaningful for human-centred fields and applications, we take a perception-based approach in simplifying and quantifying the high-dimensional light-field data. So, in this study we capture the physical light field and analyze its structure in a perception-based manner.

Light fields in natural environments are dynamic and complicated, because natural scenes usually consist of complex spaces, shapes, materials, and lighting, that optically interact with each other. Luckily, any local light field can be decomposed as a weighted sum of basic spherical functions using spherical harmonics (SH) [7–11] and a scene's light field can thereby be sampled,

#479715 https://doi.org/10.1364/OE.479715
Journal © 2023 Received 17 Nov 2022; revised 19 Jan 2023; accepted 2 Feb 2023; published 24 Feb 2023

Optics EXPRESS

described and visualized approximately via sparse measurements [10] in a simplified and intuitive manner [12]. Spherical harmonics are angular functions with increasing frequency that can be represented as monopoles, dipoles, quadrupoles, etc. (see Fig. 1 for an illustration). These functions form a complete basis for describing the variation of illumination on a sphere. This mathematical basis has an immediate optical meaning [9,13–15], and its components have been shown to be directly related to perceptual judgments [4,16,17]. The zero-order SH component is a scalar known as light density, and the SH decomposition's first coefficient represents its strength. Its physical meaning is the spectral irradiance averaged over all directions. Perceptually, it is associated with the strength of the ambient light. The first-order SH component represents the light vector, whose strength and direction can be described with three coefficients. Its physical meaning is the net spectral irradiance transport [2,9]. Perceptually, it is associated with the strength and direction of a directional source. Deducting the contribution of the vector component from the illumination solid gives an estimate of the symmetric component [8,18]. The symmetric component has the property that, for any plane passing through the measurement point, it produces equal irradiance on opposite sides. The second-order SH component is the squash tensor [9], requiring five coefficients. It can be considered as a light or dark clamp. The third- and higher-order SH components can be summarised statistically to represent the "brilliance" or "light texture" of the light environment [19].

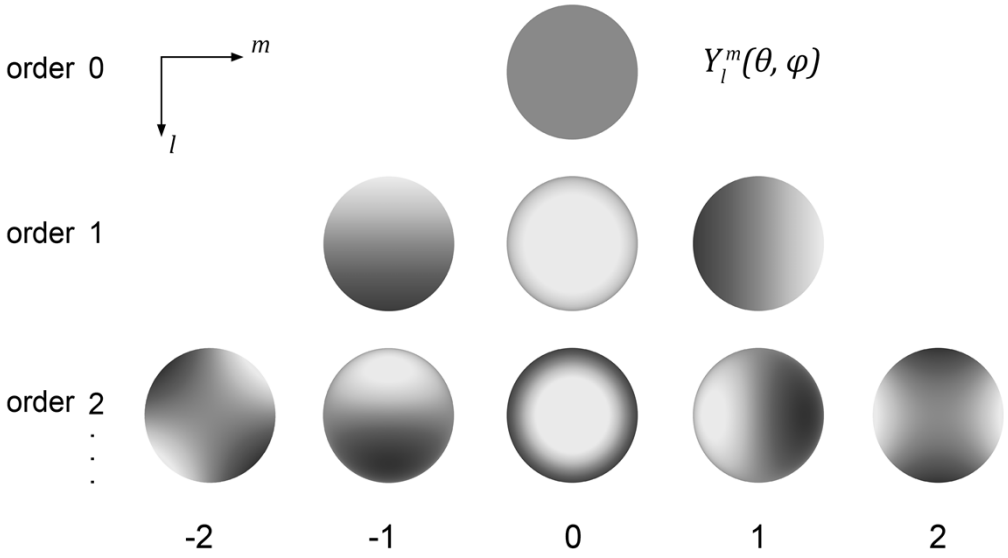

Fig. 1. Real spherical harmonics of orders 0, 1, and 2, corresponding to first nine basis functions. The front of the sphere is shown, with white to light gray representing positive values and black to dark gray representing negative values. These images show the real form of the spherical harmonics. The connection between these functions and Gershun's theory is explained in detail in the work of Mury et al. [9–11].

Recently, progress has been made in measuring the optical light field. In several studies, the light field was captured using imaging or photosensor systems (Table 1). In the imaging approach, a digital camera is used to either photograph the environment directly [20] or indirectly via the reflection of the environment from a mirror sphere [11,21,22]. An advantage of these approaches is the high angular resolution. Direct photographing requires a digital camera equipped with a fisheye lens and rotation tripod. Such cameras typically possess only three spectral channels, *i.e.* red, green and blue (RGB) [20]. This coarse spectral resolution might not always be sufficient for accurate colorimetric description [14,23,24]. A (hyper)spectral camera provides a spectrally

Optics EXPRESS

resolved solution [21]. However, taking a single hyperspectral image is time-consuming and thus this method cannot be used to capture fine temporal variations. Additionally, both imaging approaches have the disadvantage that the extremely high dynamic range (HDR) of natural exterior light environments often exceeds these devices' capturing ranges, and then need photos with multiple exposures to cover the environments' ranges. This is impossible in dynamic scenes because the light will change between different photos. Moreover, it results in relatively large measurement errors.

Table 1. Studies that employed light-field methods to characterize the light environment[a]

Studies	Light-field aspects taken into account							
	HDR⋮		Temporal resolution‡		Spectral resolution*		Directional resolution⁞	
Morimoto et al. [21]	-	2250:1 (11 stops)	-	40 minutes per spherical image	Hyperspectral	400-720 nm in 10 nm interval	✓	∞⁂
Li et al. [22]	-	400:1 with 2 integration times	-	up to 90 minutes per spherical image	Hyperspectral	400-1000 nm in 7 nm interval	✓	∞
Nilsson et al. [20]	-	2 orders with 3 integration times	-	Up to 68.5 minutes per spherical image	Multispectral	RGB¨	✓	∞
Adams et al. [30]	✓	63096:1 (26 stops)	-	up to 24 minutes per spherical image	Multispectral	RGB	✓	∞
Mury et al. [10]	✓	7 orders	✓	Real-time (1 second)§	Monospectral	Luminance	✓	SH order 2
Morgenstern et al. [31]	✓	5 orders (ranging from low-lit indoor scenes to direct sunlight)	✓	Real-time (1 second)	Monospectral	Luminance	✓	SH order 2
Xia et al. [27]	✓	7 orders (0.01-299900 lux)	✓	Real-time (1 second)	Monospectral	Luminance	✓	SH order 1

[a]– denotes exclusion.
✓ denotes inclusion.
⋮ Order of HDR means the order of magnitudes of the dynamic range.
‡ The temporal resolution is given for a measurement at a single location and the spatial resolution is ignored in this table.
* Mono-, multi- and hyperspectral refer to a single band, 3 to 10 wide bands and hundreds of narrow bands [32–34], respectively.
⁞ SH order means the order to which the spherical harmonics can be estimated.
⁂ The notation ∞ at directional resolution should be interpreted as a very high angular resolution that is limited by the number of pixels in the panoramic image.
§ Multidirectional photosensors arranged in a spherical configuration offer the ability to simultaneously measure the entire solid angle without the need for time-consuming reorientation.
¨ RGB is here used as a coarse representation of the visible spectrum [24], divided into Red, Green and Blue bands, with Red typically around 568-700 nm, Green around 482-568 nm, and Blue around 400-482 nm, and dominant wavelengths of 457, 530, and 597 nm respectively.

Omnidirectional photosensor systems combine many photosensors to capture the irradiance in all directions. Such a system provides a low-angular-resolution but high-dynamic-range, and real-time measurement of the local light field. Several researchers built such omnidirectional devices with varying numbers of sensors [8,9,25] but no spectral resolution. Connected to this

Optics EXPRESS

approach is the question of how many sensors are needed to measure the light field in a certain angular resolution, while keeping the information tractable. The SH description provides a fundamental basis for understanding what is needed depending on the objectives. The minimal number of sensors needed equals the total number of coefficients required for the order of the mathematical description of the local light field, *e.g.* one needs at least four sensors to estimate the first-order SH description and at least nine for the second-order approximation. Ramamoorthi et al. [26] proved formally that a second-order SH approximation of local illumination suffices to describe the appearance of convex matte objects, since the bidirectional reflectance distribution function (BRDF) of matte material acts as a low-pass filter on directional variations in the light field. In most natural scenes, diffuse scattering dominates in the material BRDFs. Much of the light field is then dominated by diffuse scattering [9], causing it to behave smoothly, and allowing capturing by sparse measurements [10]. It is thus sufficient to quantify the light environment of a diffuse scene or a scene dominated by diffuse scattering via a second-order light-field approach. A dodecahedron-shaped plenopter equipped with 12 evenly distributed sensors can measure a second-order approximation of the light field [9]. However, the resulting second-order squash tensor may be difficult for non-experts to interpret. Xia et al. [27] used a custom cubic apparatus with six sensors to robustly measure the first-order approximation of the light field. Their first-order SH decomposition [8] includes only the light density and light vector, and they found that Cuttle's approach [18,25,28], using a set of simple linear functions, can be used to estimate the same metrics. A first-order light field approach is able to explain 94% of matte object appearances [29] or diffuse scattering, making it a practical and effective choice for descriptive purposes. Moreover, this description captures the key elements of the subjective correlate of the light field, the visual light field [6,13]. However, in environments with multiple highly directional light sources or strong reflections, higher-order components may be necessary to predict fine details of the appearance of the environment and especially objects with spiky reflectance functions such as shiny materials.

In this paper, we extended the cubic system to a spectral HDR cubic illumination system to capture up to the first-order spectral local light fields. The system is portable and suitable for field research. We also show how perception-based metrics can be derived from the cubic samples, to capture spectral, angular, temporal and spatial variations of effective daylight. We demonstrate the approach with measurements of data sets collected in natural exterior scenes. We found that the differential chromatic effects for the different light-field components in natural scenes were large. In our test cases, the spatial and temporal variations in illuminance and color characteristics were the largest for the light vectors, medium for the light densities, and smallest for the symmetric component. Moreover, this approach allows capturing wavelength-dependent directional variations that we discuss to have important implications for predicting color gradients in the appearances of objects and scenes. Our main contribution thus exists of the extension to the spectral domain under challenging HDR conditions, and showing how the complex 7-dimensional light field data can be captured and transformed into perceptually relevant information.

2. Methods

Despite the fact that solar radiation is more or less static, effective daylight is dynamic. Earth's axial tilt along with rotation and revolution, complex atmospheric optical effects and the presence of occluders and mutual reflections cause variations in an observed effective daylight field [35–37]. We aimed to quantify temporal, spatial, angular and spectral variations of the effective light field in natural scenes by cubic measurements (spectrometers configured on the faces of a small cube). In order to quantify this complicated 7D function in a meaningful manner for humans, we convert the raw radiometric cubic data to perception-based light components and photometrical measures. In the subsections hereafter, we describe the cubic measurement systems, the data processing pipeline, and the two empirical studies.

Optics EXPRESS

2.1. Spectral cubic illumination measurement

The spectral cubic irradiance was measured using two types of systems. The first system was relatively affordable and consisted of a portable handheld spectrophotometer (Sekonic C-7000, made in Japan in 2015) and a microscopic reference cube made of spectrally neutral white resin. Cubic measurements were done by placing the spectrophotometer consecutively on the cube's six faces and recording the spectral irradiances. The second system for measuring spectral cubic irradiance was a remotely addressable irradiance spectrophotometer (Konica Minolta CL-500A, made in Japan in 2011) mounted on a three-axis angle-adjustable tripod (shown in Fig. 2(b)). The tripod occludes 2.97% of the entire solid angle. A laptop (Dell Latitude 7410) drove the irradiance spectrophotometer from a distance through an 8-meter-long USB cable via Data Management Software CL-S10w. The meter was oriented to all six cubic faces by adjusting the tripod. The operator then triggered and recorded the spectral irradiance measurement of each direction via the laptop.

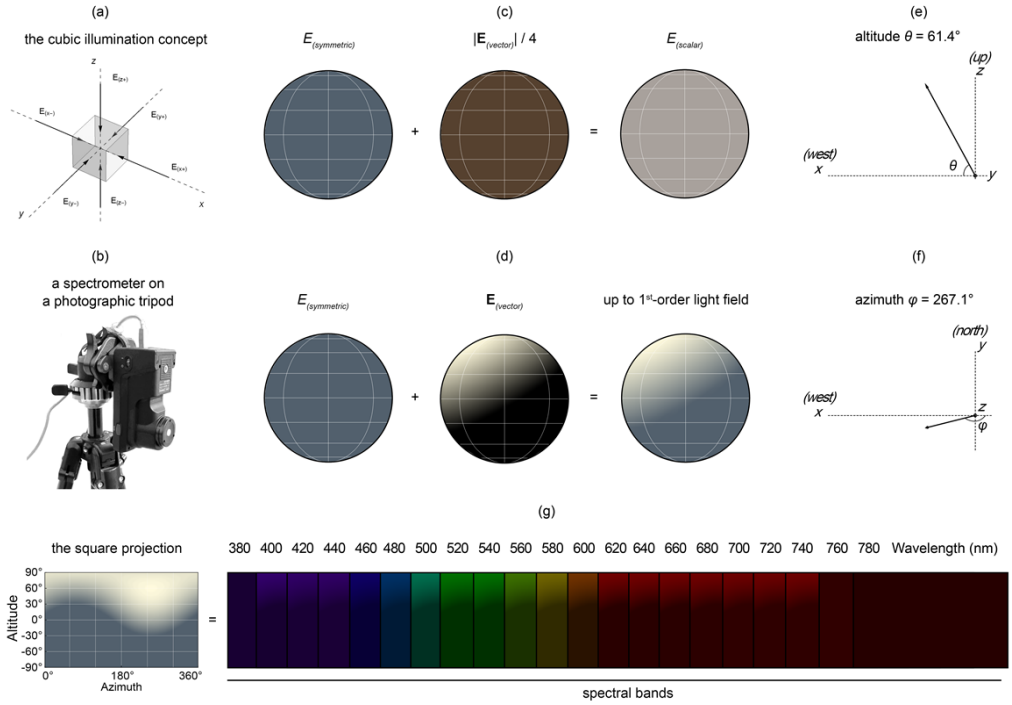

Fig. 2. Quantification of up to the first-order light field with the spectral cubic illumination method measured outdoors in the afternoon. (a) Six spectral irradiances on the faces of a small reference cube define the spectral cubic illumination (local light field). (b) The spectrophotometer mounted on a tripod to capture spectral cubic illumination. (c) The symmetric and vector components' magnitudes add up to the light scalar. (d) The symmetric component's magnitude plus the light vector gives up to the first-order light field. (e) The altitude of the light vector. (f) The azimuth of the light vector. (g) Representation of the square-projected illumination map, computed independently for each wavelength. Here we show 21 spectral bands from 380 nm to 780 nm in an increment of 20 nm for simplification. See Fig. S1 of Supplement 1 for a 360-degree panoramic view of the surrounding measurement environment.

The cube or tripod was aligned with the positive direction of the y-axis pointing North, and the positive direction of the z-axis facing upwards. Thus, the Cartesian coordinate system of the

Optics EXPRESS

spectral cubic irradiance was oriented according to the principal directions in the geographic coordinate system. A compass was used to calibrate the orientations.

Dark calibrations were performed prior to the acquisitions. The spectral irradiance measurement was acquired over a wavelength range from 380 nm to 780 nm in 11 nm intervals for the Sekonic C-7000 and 360 nm to 780 nm in 10 nm intervals for the Konica Minolta CL-500A. The cubic measurements lasted one minute in daylight to five minutes at dawn and dusk. The Sekonic C-7000 can capture the irradiance over a dynamic range of five orders of magnitude (1 to 200,000 lux), and the Konica Minolta CL-500A of six orders (0.1 to 100,000 lux). The Sekonic C-7000 allows for fast reorientations, and thus it is suitable for spatial light-field measurements in an unstable light environment. The Konica Minolta CL-500A has the advantage of allowing measurements of dim light environments and remote control, minimizing the effects of (inter-)reflections from the operator. The operator was dressed in black to reduce the influence from (inter-)reflections as much as possible.

2.2. Data processing and analysis

2.2.1. Basic components of the light field

Estimates of the spectral light-field components were derived as follows. The systems give spectral cubic data, namely $\mathbf{E}_{(\lambda,x+)}$, $\mathbf{E}_{(\lambda,x-)}$, $\mathbf{E}_{(\lambda,y+)}$, $\mathbf{E}_{(\lambda,y-)}$, $\mathbf{E}_{(\lambda,z+)}$ and $\mathbf{E}_{(\lambda,z-)}$ [25,38] (Fig. 2(a)). The cubic measurements $\mathbf{E}_{(\lambda,x+)}$ and $\mathbf{E}_{(\lambda,x-)}$ represent the opposed pair of spectral irradiances along the x-axis (East and West), and analogous for the y (North and South) and z axes (up and down). The spectral irradiances of the light-vector components in the x, y and z directions were estimated by subtracting the associated opposed paired measurements, respectively. For example, on the x axis,

$$E_{(\lambda,x)} = E_{(\lambda,x+)} - E_{(\lambda,x-)}. \tag{1}$$

The light vector is defined as

$$\mathbf{E}_{(\lambda,\mathrm{vector})} = [E_{(\lambda,x)}, E_{(\lambda,y)}, E_{(\lambda,z)}]. \tag{2}$$

The magnitude of the light vector in spectral irradiance, then is

$$|\mathbf{E}_{(\lambda,\mathrm{vector})}| = \sqrt{E^2_{(\lambda,x)} + E^2_{(\lambda,y)} + E^2_{(\lambda,z)}}. \tag{3}$$

The magnitude of the symmetric sub-component $\sim E_{(\lambda,x)}$ equals the magnitude of the lesser of $E_{(\lambda,x+)}$ and $E_{(\lambda,x-)}$,

$$\sim E_{(\lambda,x)} = \frac{E_{(\lambda,x+)} + E_{(\lambda,x-)} - |\mathbf{E}_{(\lambda,x)}|}{2}. \tag{4}$$

The mean of the symmetric sub-components for the three axes gives a measure of the magnitude of the symmetric component.

$$E_{(\lambda,\mathrm{symmetric})} = \frac{\sim E_{(\lambda,x)} + \sim E_{(\lambda,y)} + \sim E_{(\lambda,z)}}{3}. \tag{5}$$

The light density is defined as the average spectral irradiance from every direction. It equals Cuttle's light scalar, the sum of the symmetric component and weighted light vector magnitude, up to a normalization constant [8].

$$E_{(\lambda,\mathrm{scalar})} = E_{(\lambda,\mathrm{symmetric})} + \frac{|\mathbf{E}_{(\lambda,\mathrm{vector})}|}{4}. \tag{6}$$

The linear combination of the symmetric and vector components forms a spherical harmonics (SH) approximation of the illumination map up to the first order, as shown in Fig. 2(c-d). It is

Optics EXPRESS

important to note that the symmetric component is actually a spherical distribution which is generally not uniform, but in practice can be defined adequately by its magnitude [39]. Research by Xia et al. has shown that Cuttle's scalar-vector approach provides the same information as the SH density-vector approach, with some normalization constants applied. Each of these components can also be spectrally resolved, as demonstrated in Fig. 2(g). It is worth mentioning that the illustration here uses 21 spectral bands with a 20 nm increment, but the number of bands can be as large as the equipment's resolution capabilities.

The photometric values of the components were calculated in the following way. The inner product of the luminosity function $\bar{y}_{(\lambda)}$ with the spectral irradiance over the visible spectral range gave their illuminance, as below for the x-direction.

$$E_{(x)} = 683 \cdot \int_{\lambda=380}^{780} \bar{y}_{(\lambda)} E_{(\lambda,x)} d\lambda. \tag{7}$$

For each of the metrics, the corresponding CIE tristimulus values, (x,y) chromaticity coordinates and CCT were calculated according to standard methods [40]. We used the CIE physiologically relevant 2-degree photopic luminosity function and the CIE standardized 2015 2-degree XYZ color matching functions [40,41] to perform these calculations.

The vector altitude (θ) and azimuth angles (φ) were derived from the direction of the light vector, which is entirely determined by $(E_{(x)}, E_{(y)}, E_{(z)})$ in Cartesian coordinates (see Fig. 2(e-f)). Thus,

$$\theta = \tan^{-1} \frac{E_{(z)}}{\sqrt{E_{(x)}^2 + E_{(y)}^2}} \tag{8}$$

$$\varphi = \tan^{-1} \frac{E_{(y)}}{E_{(x)}}. \tag{9}$$

The light diffuseness [8] was defined as one minus the ratio between the light-vector and light-scalar magnitudes divided by 4 and ranges from 0 for fully collimated light to 1 for spherically diffuse or Ganzfeld light.

$$D_{normalized} = 1 - \frac{|\mathbf{E}_{(vector)}|}{4E_{(scalar)}}. \tag{10}$$

2.3. Measurements of natural light fields

Our proposed approach allows for measuring 7D light fields in any scene in real time. This however would need a matrix of cubic systems to be operated remotely. In practice, financial limitations made it necessary to split our measurements into two experiments, showing spectral and directional variations as a function of space in one experiment, and as a function of time in the other experiment.

In Experiment 1 (spatial experiment), we aimed to capture and compare spectral and directional variations of the daylight field over space. Therefore we chose to compare the light field in direct sunlight and in shadow parts of exterior scenes. We took cubic measurements of natural outdoor scenes during daytime in July 2020 and August 2021 at multiple locations around the Delft University of Technology campus (52.0116° N, 4.3571° E; elevation 0 m), located in the Northern hemisphere, on sunny days with a blue sky, around noon. A total of 24 natural scenes were selected. The scenes included a variety of colored surfaces in both rural and urban settings. They were chosen to contain surfaces that were partly lit by sunlight and partly in the shade as to capture two light zones [42,43] in the light field. In each of the 24 scenes, the local light fields of the sample points in the light and shade were acquired within 1 minute, yielding a total of 48 local light field measurements. The acquisition was done via the Sekonic C-7000. For illustration purposes, we also photographed all scenes via a Canon EOS 5D Mark II camera as raw images with a constant 5500 K white balance, matching to average noon daylight.

Optics EXPRESS

In Experiment 2 (temporal experiment), we aimed to capture temporal variations over the day for a sunny and a cloudy day. We used the Konica Minolta CL-500A device to collect local light fields from a rural location (51.9795° N, 4.3850° E; elevation 0 m) in the Delft region of the Netherlands at a 5-minute interval from dawn to dusk on September 22 in autumn and on December 8, 2021 in winter. The location was an area where anthropogenic light sources were minimal for exclusive characterization of effective daylight. The sky on the first day was clear, while that on the second day was cloudy with strong wind. The full-day measurements took place within the just-before-dawn to just-after-dusk periods of 06:30–20:15 in September and 07:20–17:40 in December. In total, 165 cubic measurements were collected on the sunny day and 124 on the cloudy day (the daytime was shorter in winter). Meanwhile, we also used a spherical camera (Panono Camera) to capture HDR illumination maps at a 60-minute interval for visual illustration.

In our study, we used two systems for measuring spectral cubic irradiance: the Sekonic C-7000 and the Konica Minolta CL-500A. The Sekonic C-7000 was used in Experiment 1, where fast reorientation was needed in a complex dynamic environment. The Konica Minolta CL-500A was used in Experiment 2, where a high dynamic range was necessary for measuring dim light environments. These systems were chosen to effectively address the unique challenges presented in each scenario, and by using them together we were able to gather more accurate and reliable data to analyze the light environment.

Dataset 1, [44] contains raw spectral cubic illumination measurements of both experiments, which are made freely available.

3. Results

3.1. Experiment 1: spatial variations of chromatic light fields in natural scenes

In Fig. 3, we show the photographs of the measured scenes, showing that sunlit parts appeared brighter with more directed yellowish light and shadow parts appeared darker with more diffuse blueish light. We can also see clear effects on the appearance of the scenes. For example, in Scene 12, the color appearance of the slender vervain flower was reddish magenta in the light but blueish purple in the shade. The step between the cast shadow and the illuminated area did not just form an illuminance edge but also a chromatic edge (see Fig. S2 of Supplement 1 for detailed results).

In order to visualize the results, a light probe, a white Lambertian sphere [6], was superimposed on a photograph of the location where the cubic measurement was taken. The appearance of the probe was then rendered under each approximated illumination map derived from the cubic measurements. For ease of understanding, the spectral images of the rendered probes were then converted to RGB color images. Additionally, a gamma value of 2.2 was applied to the linearized rendered spheres for display on a screen. Please note that only six spectra per image were considered, which corresponds to the six facets of the cube. The images of the spheres presented in Fig. 2 should not be taken as actual spectral data, but rather as a reference for visualization purposes. The light probes in the cast shadow appeared bluer and darker than those in the sun. In addition, the light probes indicate a diffuseness difference between sunlit and shadowed, which causes a difference in texture contrast [45].

Figure 4(a) shows the CCT of the light-field components in the shade and light for all measured scenes. The light density CCTs in the shade (blue bars) were consistently higher than in the light (yellow bars), with an average difference of 1821 ± 1232 K (mean ± 1SD). The light vectors in shade and light had even larger CCT differences, 3542 ± 1680 K (mean ± 1SD). By contrast, the CCTs of the symmetric components in the shade were not consistently higher than in the light, and their differences were relatively small, 655 ± 1183 K (mean ± 1SD). The data presented in the form of inverse CCT can be found in Supplement 1, Fig. S3.

Optics EXPRESS

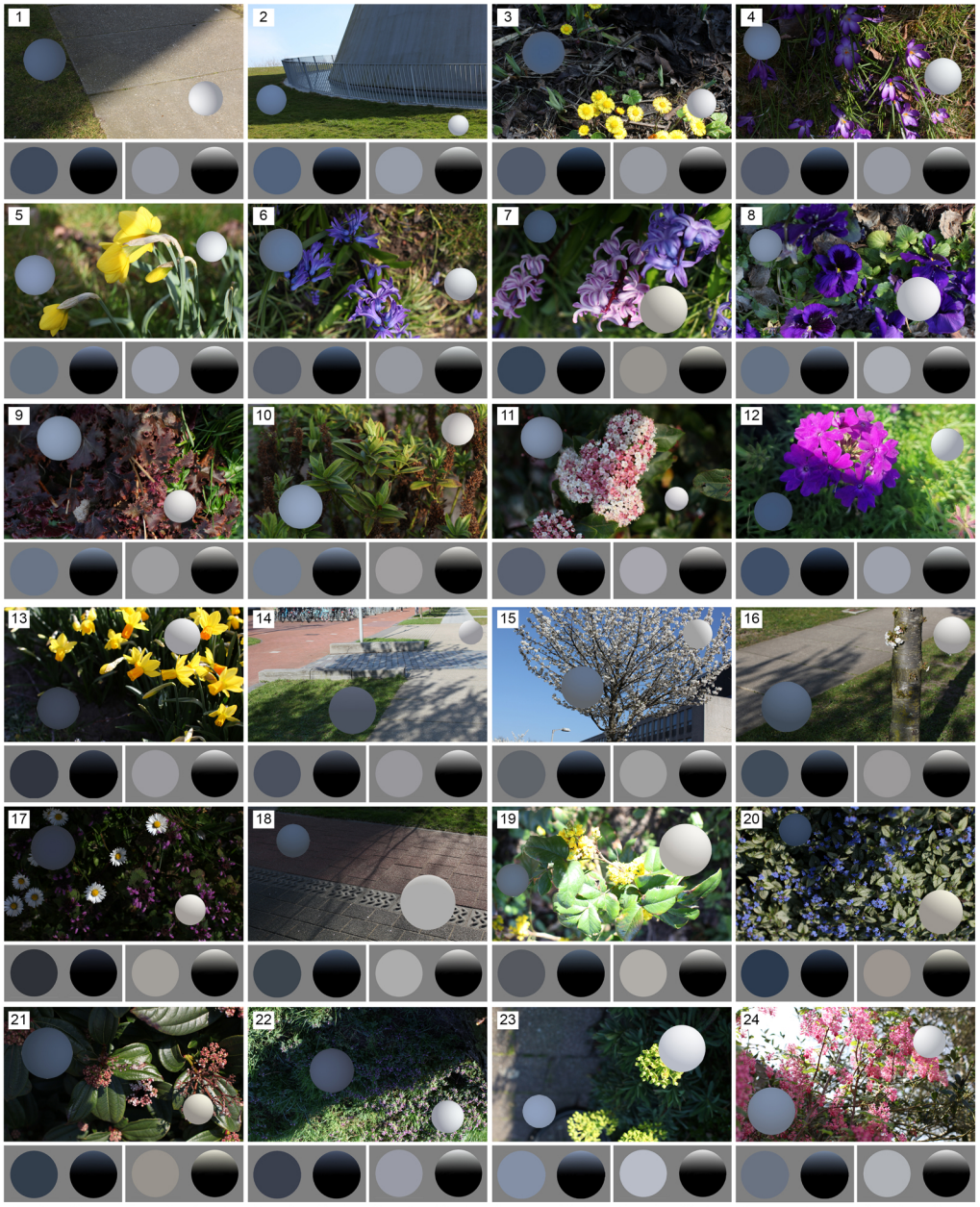

Fig. 3. The collection of all the selected natural scenes' photographs. Light probes were rendered for first-order local light field approximations as if they were embedded in the scenes. Below each scene photograph, the decomposed local light fields are shown. The light-vector directions were normalized to point upward in the decomposed light-field probe renderings. The 24 scenes were arranged from left to right and top to bottom in numerical order from 1 to 24.

Optics EXPRESS

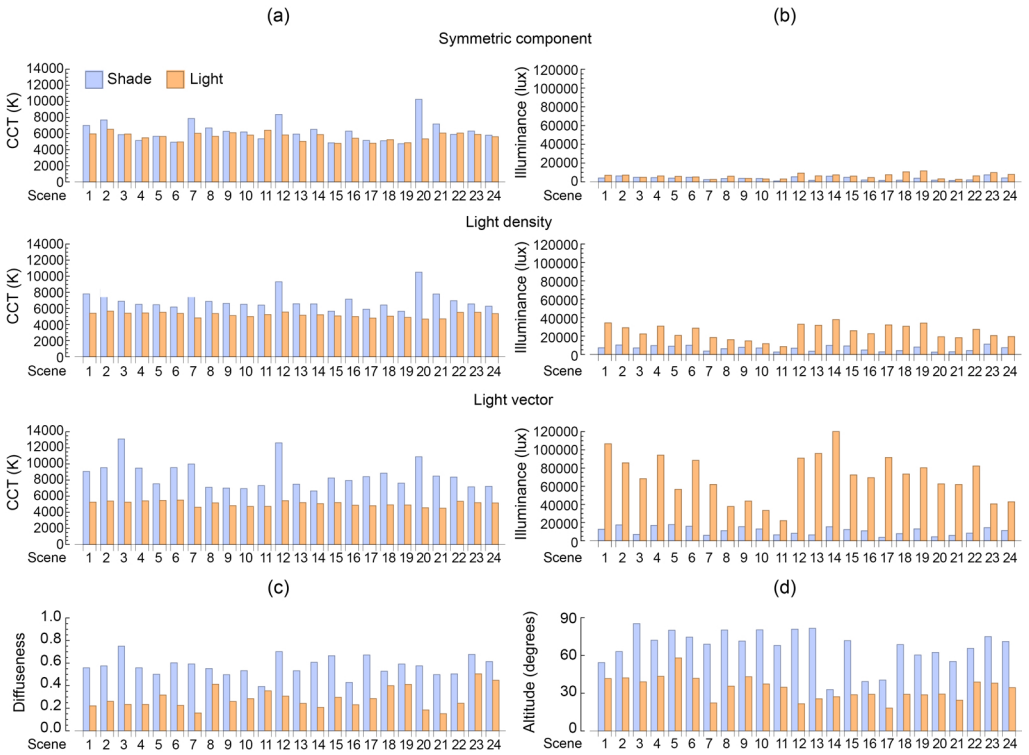

Fig. 4. The scene metrics in the shade and light. The (a) CCTs and (b) illuminance of symmetric component (top), light density (middle) and light vector (bottom) for the shade (blue bars) and light (yellow bars) regions. The (c) diffuseness and (d) altitude of the light vector for the shade (blue bars) and light (yellow bars) regions. The number on the horizontal axis indicates the scene number.

Figure 4(b) shows the illuminance of the different light-field components in the same format. The illuminance of the light densities and vectors showed considerable differences in the shade and light regions as expected, while the light vectors' differences were larger (up to five orders of magnitude, 15577–104803 lux) than for the light densities (up to four orders of magnitude, 4716–29259 lux). The illuminance differences between shadow and light for the symmetric component were smaller (up to four orders of magnitude, 12–10077 lux).

Figure 4(c) shows the measured scenes' diffuseness in the shade and light. The illuminance of the light density in the shade was relatively high compared to the light vector, resulting in overall high diffuseness values (0.4–0.8). The light vector is much stronger than the density in the light region, resulting in high directionality or low diffuseness values (0.1–0.5). The altitudes of the light vector in the shade (33° – 85°) were higher than in the light (18° – 58°), revealing an average light-direction difference (Fig. 4(d)).

Figure 5(a) shows the average spectra of the different light-field components in the shade and light. Before averaging, all spectra were converted to have equal luminous flux (CIE tristimulus value Y = 100). Overall, the spectra in the shade and light for the symmetric component showed a resemblance, with peaks in the long-wavelength part. The light-density spectra in the shade differed from those in the light, especially in the long-wavelength part. Those differences were larger for the light vector.

Figure 5(b) shows the associated chromaticities, which closely followed the daylight locus. The chromaticities of the symmetric components for shade and light regions overlapped, while

Optics EXPRESS

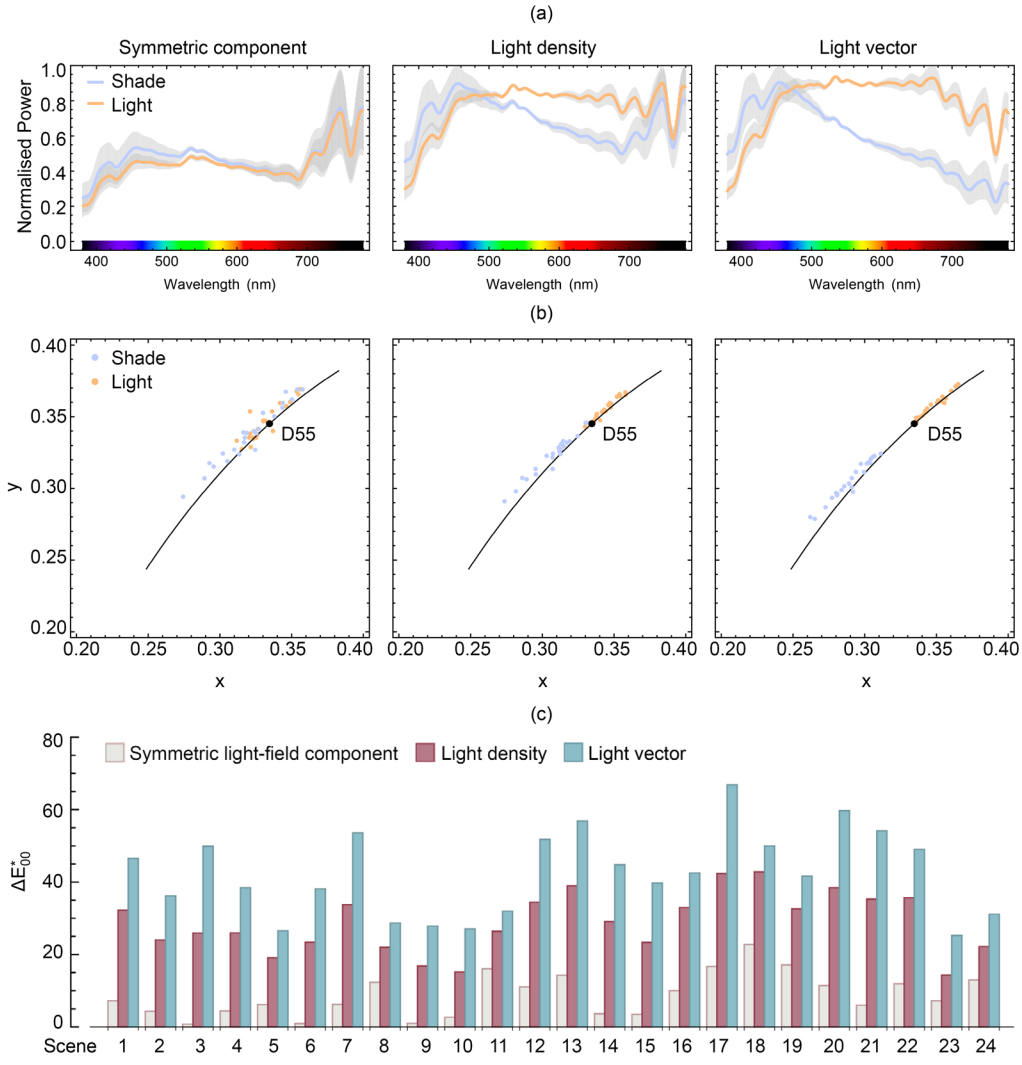

Fig. 5. Spectra and chromatic properties for the scenes of Fig. 2. (a) normalized mean spectra with the gray area depicting ± SD and (b) chromaticity coordinates of the 24 scenes for symmetric component, light density and light vector (left to right) in the shade (blue) and light (yellow) regions. The black dot represents D55 for reference. (c) Color differences (CIE ΔE2000) between the shade and light regions for the symmetric component (grey bar), light density (brown bar) and light vector (blue bar).

Optics EXPRESS

that in the shade showed a larger spread along the daylight locus towards the blue region (Fig. 5(b) left). The chromaticities of the light density of the shade and light regions separated in different clusters on the daylight locus at both sides of D55 (mid-morning or mid-afternoon daylight) (Fig. 5(b) middle), and those of the light vector were even more apart (Fig. 5(b) right).

In Fig. 5(c), we present the color differences between the shade and light conditions for the three light-field components. These color differences were estimated using the CIE $\Delta E2000$ metric in the CIELAB color space, which is known to be perceptually uniform within a reasonable approximation [46]. To calculate the ΔE values, we first converted the tristimulus CIE XYZ values derived from the light-field component spectra into CIELAB using the D50 white point. A ΔE value of 1 represents the just noticeable difference, values between 1 and 5 are considered to be discriminable when viewed adjacent, values between 5 and 10 are considered perceptible, and values greater than 10 are considered different color categories [47]. As shown in the figure, the color differences of the symmetric components (1–23) were smaller than those of the light densities (14–43), which in turn were smaller than those for the light vectors (25–67). Additionally, the color differences varied over the different scenes. The color differences of the light densities had a strong positive correlation with those of the light vector ($r = 0.91$, $p < 0.001$), as well as with those of the symmetric component ($r = 0.62$, $p < 0.001$). However, the correlation between the color differences of the light vector and symmetric component was weak and not statistically significant ($r = 0.32$, $p > 0.1$).

3.2. Conclusions experiment 1

Natural daylight constitutes a varying mix of sunlight and skylight. As demonstrated by local light-field measurements, the light densities and vectors in the shade consistently showed higher CCT and lower illuminance than in the light, and those differences for the light vectors were even larger. This was expected since the blue-rich and low luminous skylight is the prime light source in the shade, though the magnitude of the effects differs for different scenes. The CCT and illuminance of the symmetric components were found to be more or less similar in shade and light. The most credible reason is that the omnidirectional nature of (inter-)reflected light results in a relatively constant symmetric component over the scenes. Additionally, the light fields in the shade showed higher diffuseness relative to those in the light. These spatial variations in local light field illuminance, diffuseness, directions and spectral properties were found to be large. Moreover, our light-field data highlighted the differential luminous and chromatic properties for diffuse and directed components of natural light fields.

3.3. Experiment 2: temporal variations of chromatic light fields in natural scenes

Figure 6 shows the panoramic images of the scene at different times of day in a light probe format for sunny (a) and cloudy (b) weather conditions. These low-dynamic-range images are only for illustrative purposes. We can see the atmospheric features, such as clouds, and how they varied on the sunny day (Fig. 6(a)) and cloudy day (Fig. 6(b)).

3.3.1. Sunny day

Figure 7(a) shows the temporal changes in CCT on the sunny day. The CCTs of the light vector ranged from 2764–20118 K, covering a larger span than the symmetric component (3796–11364 K) (Fig. 7(a) upper row). The CCT range of the light density (3819–14544 K) was in between those ranges, as expected.

During effective daytime from 8:30 to 18:30 (when the sun appeared visible at the measurement location), the light vector CCTs expressed smooth changes from lower (3981 K) to higher (5740 K) and then back to lower (4063 K) values with an average speed (AVs) of 0.23 K/s. The light density behaved similarly, while the changes were less smooth but faster (0.25 K/s). However,

Optics EXPRESS

Fig. 6. sRGB representations of illumination maps measured at a 60-minute interval via a Panono spherical camera.

Optics EXPRESS

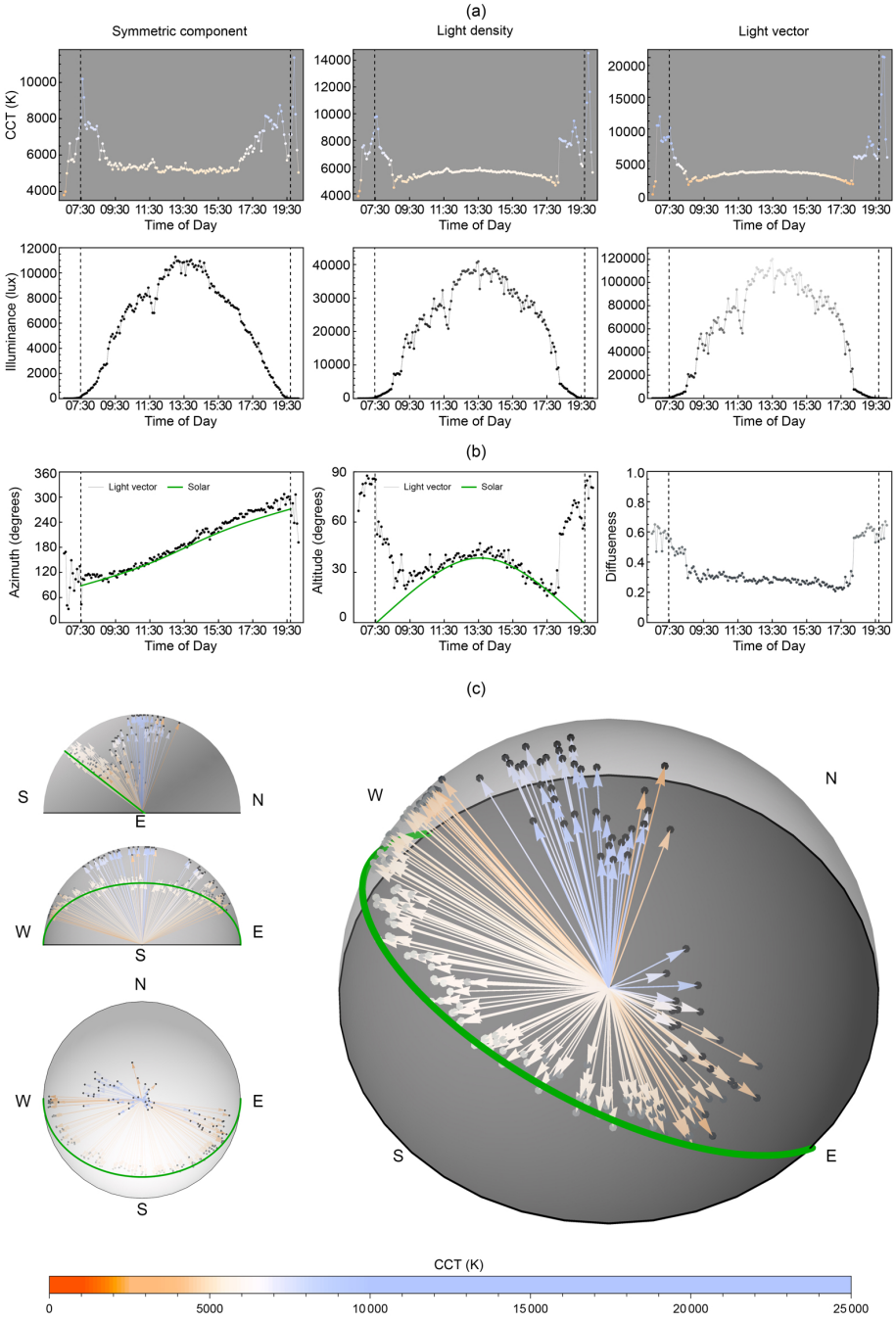

Fig. 7. Presentation of temporally-resolved spectral cubic illumination data on the sunny day. Temporal CCT (a) and illuminance (b) variations for the symmetric component (left column), light density (middle column) and light vector (right column) within the natural light field. (c) Temporal light-vector azimuth (left column), light-vector altitude (middle column) and diffuseness (middle column) variations. The black dashed lines indicate astronomical sunrise and sunset time. (d) Temporal variations of sun positions and light-vector directions. Normalized light vectors plotted as east elevation (left column first row), south elevation (left column second row), top view (left column bottom row) and orthogonal view (right). The chromaticities of the light vectors are represented by the colors of the arrows, with the bar legend at the bottom of the figure providing a reference for the corresponding CCT values. The lightness of the points at the end of the arrowheads indicate the relative luminance of the light vectors. The green path indicates the sun's movement. The data was collected at a temporal resolution of every 5 minutes. Additional data presented in the form of inverse CCT can be found in Supplement 1, under Figure S4(a) for further analysis.

Optics EXPRESS

the CCTs of the symmetric component fluctuated in a higher range (5005–7332 K) with an even faster average speed (0.51 K/s).

The effective twilight (when the sun was invisible to the measurement location) expressed extremely high CCTs, as high as 20118 K for the light vector, 14544 K for the light density and 11364 K for the symmetric component. The fastest CCT changes occurred at effective sunrise (from high to low CCTs) and sunset (from low to high CCTs) rather than astronomical sunset and sunrise. During the effective twilight period, the speed of CCT changes for the light vector (3.9 K/s) was fastest relative to the light density (2.7 K/s) and symmetric component (2.1 K/s). Around effective sunrise, the transition from high to low CCTs for the symmetric component ended around 9:00, almost 0.5 hours later than for the light vector and light density. The transition from low to high CCTs during sunset for the symmetric component started 1.5 hours earlier, around 17:00, whilst the CCTs for the light vector and light density were still decreasing. Right after the effective sunrise and before the effective sunset, contrary to the warm light vector, the symmetric component at ground level was bluish and diffuse. Additional data presented in the form of inverse CCT can be located in Supplement 1, under Figure S4(a).

Figure 7(b) shows the temporal changes in illuminance on the sunny day for the three light-field components. These showed synchronous temporal patterns, rising at the beginning of the day to its peak around noon, followed by a decrease in the afternoon (Fig. 7(a) lower row). The illuminance of the light vector was consistently higher, ranging from 0.2 to 120220 lux, than the light density (0.2–40912 lux) and symmetric component (0.1–11278 lux). The speed of the light-vector illuminance changes was also the fastest (15.4 lux/s) relative to light density (4.4 lux/s) and symmetric component (0.8 lux/s).

Figure 7(d) shows the hemispherical plots of the light vectors against the sun path of that day. The light-vector directions closely follow the sun path during the effective daytime, while those of effective twilight pointed upward (see also Fig. 7(c) left two columns for the corresponding angles). The effective daytime light diffuseness was low with minor fluctuations and slightly dropped from 0.370 to 0.208 (Fig. 7(c) right column). By contrast, the diffuseness of the effective twilight was up to 3 times higher, ranging from 0.444 to 0.669. The light-vector altitude and the diffuseness correlated ($r = 0.873$, $P < 0.001$) (Fig. 9(a)). From Fig. 7(b-c) right column, we can observe slight asymmetries of the vector's magnitude and the light diffuseness between morning and afternoon.

3.3.2. Cloudy day

The day length shortened on the cloudy day, and the clouds periodically occluded the sun. Figure 8(a) shows temporal changes in CCT on the cloudy day. Throughout the whole day, the CCT ranges for the symmetric component (5122 K to 21408 K), light density (4218 K to 20625 K) and light vector (3853 K to 20500 K) were large.

Over effective daytime between 9:30 to 16:00, the CCT of the light vector ranged from 3853 k to 10170 k and fluctuated more than light density (4218 K to 10210 K) and symmetric component (5122 K to 10243 K) (Fig. 8(a) upper row). The symmetric component expressed relatively higher CCT than the light vector around effective sunrise and sunset when the sun was present without cloud occlusions. The CCT difference between the symmetric and vector component was large at sunset (up to 5757 K at 15:40) and still considerable at sunrise (up to 1269 K at 09:30). The light vector showed larger and faster (2.7 K/s) CCT changes than the light density (2.4 K/s) and symmetric component (1.5 K/s) during effective daytime.

The effective twilight metrics were all rather bluish with a maximum CCT of 21408 K. Approaching the effective sunrise (9:30) and sunset (16:00), there were the fastest CCT changes for the light vector (4.6 K/s), light density (4.2 K/s) and symmetric component (3.7 K/s). Further data presented in the form of inverse CCT can be found in Supplement 1, within Figure S4(b).

Optics EXPRESS

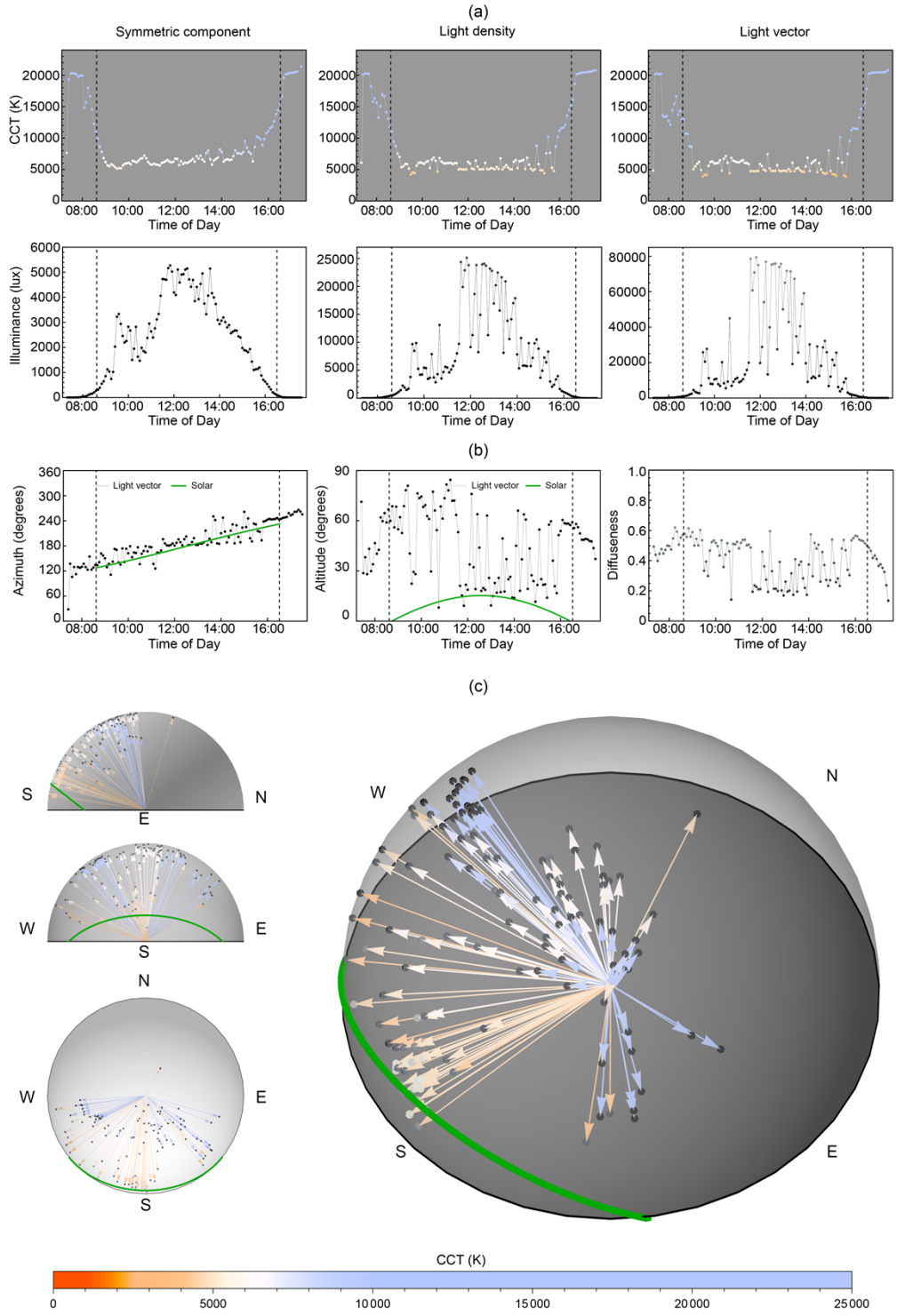

Fig. 8. Presentation of temporally-resolved spectral cubic illumination data on the cloudy day. The figure configuration is the same as Fig. 7. Additional data presented in the form of inverse CCT can be found in Supplement 1, under Figure S4(b) for further analysis.

Optics EXPRESS

Figure 8(b) shows the temporal changes in illuminance on the cloudy day. The illuminance of the light vector was consistently higher (0.02–79411 lux) than of the light density (0.006–25125 lux) and symmetric component (0.0002–5273 lux). The values were lower than for the sunny day, and also fluctuated more, together, resulting in faster changes. The average speed for the light vector was the fastest (31.5 lux/s), followed by the light density (8.3 lux/s) and symmetric component (0.9 lux/s).

As Fig. 8(b) the left column shows, the light-vector azimuth closely aligns with the sun position during the astronomical daytime. However, the light-vector altitude did not (Fig. 8(b) middle). Effectively, the light-vector directions do not correspond to the sun positions (Fig. 8(d)). Figure 8(b) right shows the diffuseness ranging from 0.135–0.620 with frequent fluctuations. Although these fluctuations look random, in Fig. 9(b), we see that the light-vector altitude and diffuseness showed strong correlations ($r = 0.821$, $P < 0.001$).

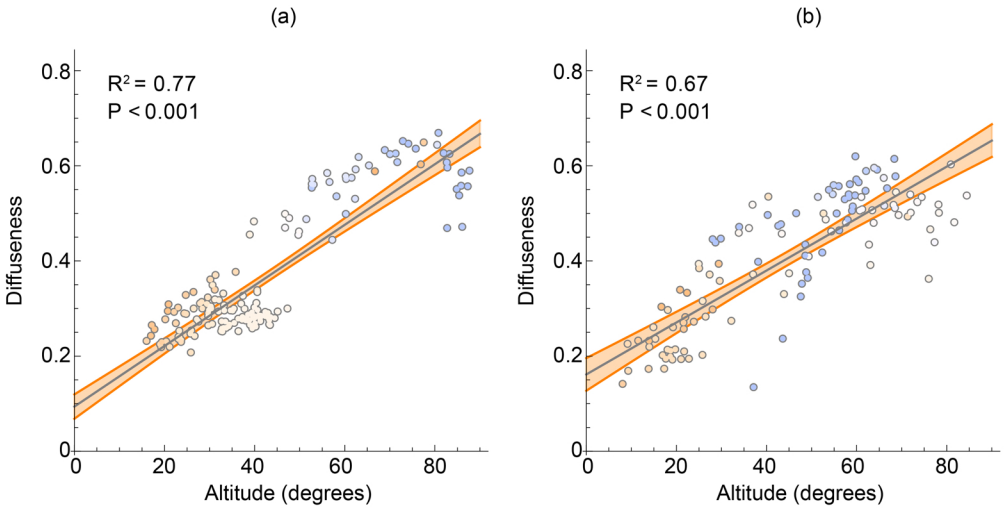

Fig. 9. The scatterplots and correlations between light-vector altitude and diffuseness for the sunny day (a) and cloudy day (b). The area around the fitted lines represent the 95% CI. Disk colors approximately represent light-vector chromaticities.

3.4. Conclusions experiment 2

Natural light (including both twilight and daylight) changes temporally in terms of CCT, illuminance, diffuseness and directions over the day. On both sunny and cloudy days, the CCT of all the light-field components expressed two blue spikes during dawn and dusk. For the effective daytime, the light-vector CCT changes on the sunny day showed a bell-shaped curve. On the cloudy day, this was disrupted with major fluctuations. The symmetric component showed relatively stable CCTs at a near-neutral white level (~D55) for both weather conditions, while the CCTs were overall higher and fluctuated more on the cloudy day than the sunny day. Again, a credible reason for its stability is that the omnidirectional nature of (inter-)reflected light results in a relatively constant symmetric component over the scenes. A plausible explanation for the higher CCT is that it also diffuses out the separate contributions from the yellowish sun and bluish sky. Additionally, overcasts are far from spectrally neutral transmitters [48] causing a bluer ambience than the sunny day. Light-density CCTs behaved more similarly to the light vectors than the symmetric component, which can be explained by the light-vector contribution to the density. The temporal profiles of the illuminance changes showed similar patterns (a bell-shaped curve) for the sunny and cloudy days. On the cloudy day, the illuminance fluctuated around the

Optics EXPRESS

characteristic temporal profile. The temporal diffuseness changes correlated with light-vector altitude changes. This can probably be attributed to direct sunlight being present or absent. When the sun is behind the clouds or below the horizon, the diffuse skylight becomes the prime light source causing high diffuseness and light-vector altitude relative to sunlight-present conditions. The measurements revealed large variations in CCT and illuminance of natural light over the days, and the temporal profiles for the different light-field components showed differential effects under both sunny and cloudy weather conditions.

4. Discussion

In experiment one, we measured up to the first-order light fields in the shade and in the light for 24 sunlit rural and urban scenes across multiple days. Spectrally dependent Rayleigh scattering causes low-luminance highly diffuse bluish skylight and high-luminance highly directional yellowish sunlight during daytime, which was confirmed by the data. The spatially varying contributions from skylight and sunlight caused large CCT, illuminance, diffuseness, direction and color differences between light and shade locations. In the shadowed parts of a scene, the diffuse light from the blue sky has the largest gain. The light field in the shade thus had much lower illuminance, higher CCTs and higher diffuseness relative to that in direct sunlight. These variations were found to be of the same prominence as the well-known temporal variations of daylight [49–51]. The spatial variations in terms of both illuminance and CCTs were larger for the light vectors than the light densities and symmetric components. We found experimentally that the symmetric component of the light field was rather constant over the scenes. This is consistent with Mury et al.'s study on light field constancy [11], which shows most materials diffusely scatter light causing relatively stable low-order components.

In experiment two, we measured spectral light fields throughout a sunny and cloudy day with 5-minute intervals. The different light-field components showed differential CCT and illuminance variations as a function of time. The light vector changed more in magnitudes of CCT and illuminance than the light density, and again than the symmetric component. The magnitude differences between different light-field components were smaller on the cloudy than sunny day, and this is presumably due to diffusion by the clouds. The light-field components expressed high CCT during the effective twilight period. This can be explained by Chappuis absorption [37,52,53] due to Ozone, inducing a progressive enrichment in the blue end of the spectrum (<500 nm) for the primary lighting. The slight asymmetries of the vector's magnitude and the light diffuseness between morning and afternoon on the sunny day might be attributed to Mie scattering by water droplets in the morning [54–58]. On the cloudy day the temporal variations were too large to signal such asymmetry.

The light-vector directions followed the sun's positions on the sunny day when the diffuseness was low. The misalignment of the light-vector directions and sun positions might be due to occlusion. High light-vector altitudes occur when the sun is absent from the measuring devices, including during twilight time and overcast conditions. The primary illumination then comes from the hemispherically diffuse skylight, resulting in high diffuseness and the observed positive correlations between light-vector altitude and diffuseness.

Those measurements however can be analyzed even further with regard to the spectral and directional properties. In Fig. 10(a), we present a detailed analysis of the light vectors measured at 18:10 on the sunny day (close to effective sunset when the sun appears at a low angle in the sky) in Experiment 2. The light vector direction is shown, which was computed based on the photometric values of the luminance channel, in line with the methodology used in the analysis of our experiments. In reality, the light-vector directions might also be wavelength-dependent, especially around sunset and sunrise. Figure 10(b-d) shows the light vectors sampled at different levels of spectral resolution, including multispectral (3 bands), hyperspectral (21 bands), and full spectral (401 bands) in the visible spectrum. The wavelength-dependent light vectors have similar

Optics EXPRESS

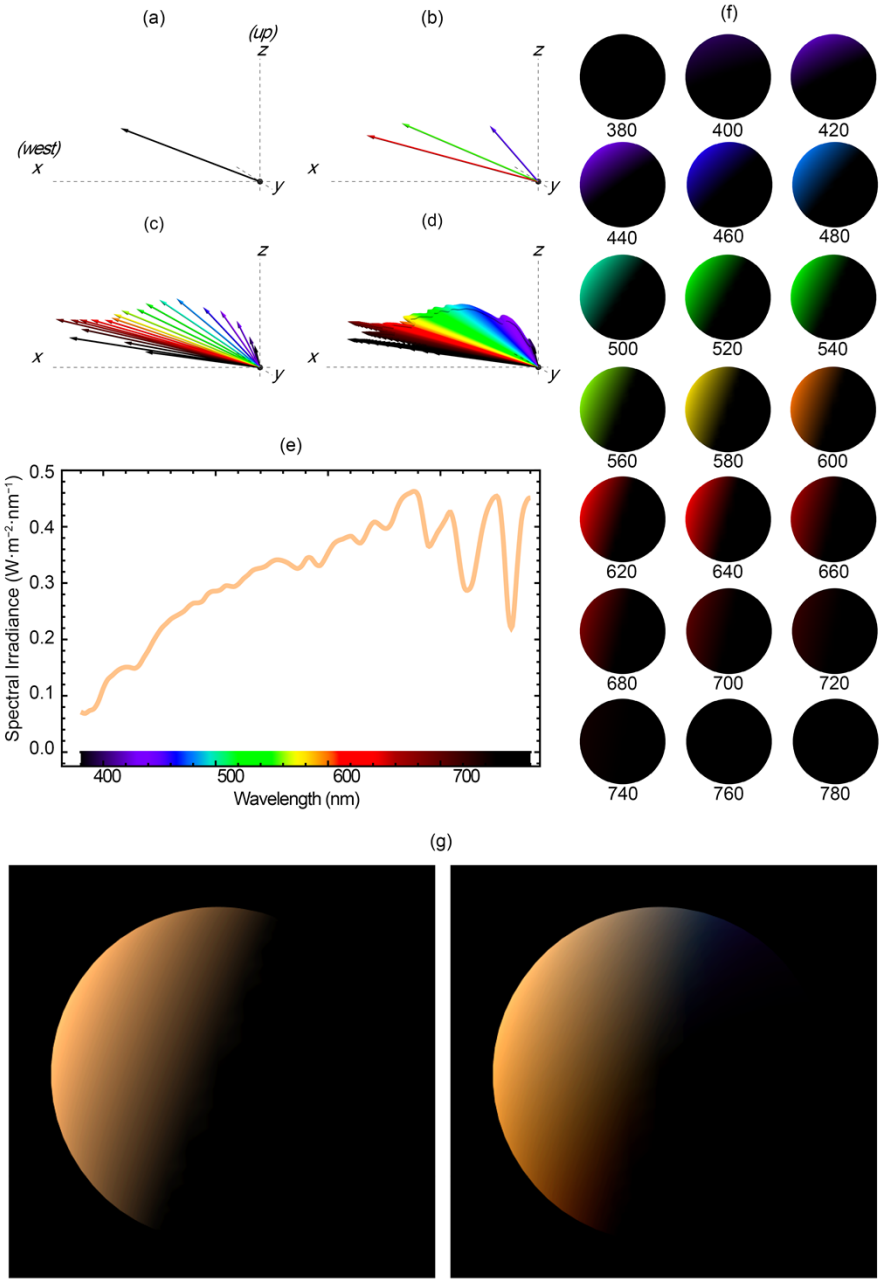

Fig. 10. Spectral light-vector properties for a sample cubic measurement measured at 18:10 on the sunny day. The light-vector plots in Cartesian coordinates ordered from low spectral resolution to high spectral resolution, starting with the monospectral plot (a) which shows the luminance channel, followed by the multispectral plot (b) that samples the light vectors at 50 nm–120 nm intervals, the hyperspectral plot (c) that samples the light vectors at 20 nm intervals, and finally the full spectral plot (d) that samples the light vectors at 1 nm intervals, covering the wavelength range of 380 nm–780 nm. The lengths of the arrows indicate the relative radiant power. (e) The irradiance spectrum of the sample light vector (a), which is equivalent to light-vector magnitudes as a function of wavelength (d). (f) Wavelength sub-band images of a white Lambertian sphere rendered under hyperspectral light vector (c). (g) sRGB representations of spectral rendering by ignoring (left) or considering (right) wavelength-dependent light-vector directions.

Optics EXPRESS

azimuths, but the short-wavelength light vectors had higher altitudes than the long-wavelength ones. This can be explained by wavelength-dependent Rayleigh scattering resulting in the short wavelengths being scattered more than the long wavelengths. Figure 10(f) shows a white Lambertian sphere rendered under spectral light vectors ranging from 380 nm to 780 nm in 20 nm intervals. The shading induced by the spectral light vectors not only showed intensity differences but also varied in directions. The misalignment of these sub-band images can, after superposition, cause complex color gradients for object shading (Fig. 10(g) right), while such complex color gradients get lost in renderings that only consider a single, average light-vector direction based on the luminance (Fig. 10(g) left). Thus, the spectral rendering considering the wavelength dependency of light-vector directions provided more accurate color gradient estimations than just relying on average light-vector directions. In the presence of multiple direct light sources with different chromaticities, quantifying both light-vector magnitudes and directions as a function of wavelength might be necessary to predict object appearance in such detail.

In addition, we represented the symmetric component as a constant, as indicated in Fig. 2(d), instead of by its actual spherical distribution. Such simplification is adequate when the symmetric component is relatively uniform [8,18]. In the case of non-uniform symmetric components, a physically correct rendering would need to take into account the symmetric component as distribution. Furthermore, a complete representation of the symmetric component should also include its wavelength dependency for precise object color appearance estimation.

Our spectrometer system and the cubic illumination data-processing pipeline were shown to be well-suited for capturing spatial, temporal, angular and spectral variations of effective daylight. A limitation of the present study is related to the angular resolution that only suffices to quantify a light field SH description up to the first order. The second limitation is that the operator needs to manually adjust the 3D orientations of the spectrometer rather than take the multidirectional measurement simultaneously. Each spectral irradiance measurement can take approximately 0.5 seconds during daytime and 27 seconds during twilight time. A solution is to construct omnidirectional devices embedded with multiple spectrometers. The number of meters can be adjusted to the desired angular resolution or order of the SH approximation. Such a method can also further improve temporal resolutions. This will allow the measurement of additional spectral light-field datasets at different locations and times of day, seasons and weather conditions to further generalize the findings. Nevertheless, the present study provides a step toward quantifying the temporal, spatial, angular and spectral variations of the light field.

5. Conclusion

In conclusion, the combination of the geometrical structure of scenes, the presence or absence of clouds, atmospheric scattering and varying sun angles leads to large illuminance, direction, color and diffuseness differences from location to location and over time. The spectral cubic illumination method allows measuring these characteristics of effective light in the environment, providing temporally, spatially, spectrally and directionally resolved measurements. We also demonstrated how to separately analyze the differential contributions of the effective diffuse and directed day-light-field components and reveal their differential statistical properties. The spectral cubic illumination method offers a novel and convenient tool for assessing light environments, which will enable the characterization of visual signals crucial to various disciplines. Furthermore, we discussed how our method can be extended to full light field measurements of any order, and how the analysis can be extended to accurately predict natural chromatic gradients in scene appearance by incorporating the spectral dependency of light-vector directions. The dynamic nature of daylight can make it challenging to quantify fully, but our research has taken initial steps in capturing and decomposing the 7D light-field structure.

Funding. H2020 Marie Skłodowska-Curie Actions (765121).

Optics EXPRESS

Acknowledgment. We would like to express our gratitude to Ling Xia for her valuable feedback.

Disclosures. The authors declare no conflicts of interest.

Data availability. Data underlying the results presented in this paper are available in Dataset 1, Ref. [44].

Supplemental document. See Supplement 1 for supporting content.

References

1. T. Kruisselbrink, R. Dangol, and A. Rosemann, "Photometric measurements of lighting quality: An overview," Build. Environ. **138**, 42–52 (2018).
2. A. Gershun, "The light field," J. Math. Phys. **18**(1-4), 51–151 (1939).
3. E. Adelson and J. Bergen, "The plenoptic function and the elements of early vision," in *Computational Models of Visual Processing*, M. Landy and J. Movshon, eds. (The MIT Press, 1991), pp. 3–20.
4. L. Xia, S. C. Pont, and I. Heynderickx, "The visual light field in real scenes," i-Perception **5**(7), 613–629 (2014).
5. T. Kartashova, H. de Ridder, S. F. te Pas, M. Schoemaker, and S. C. Pont, "The visual light field in paintings of Museum Prinsenhof: comparing settings in empty space and on objects," Proc. SPIE **9394**, 93941M (2015).
6. J. J. Koenderink, S. C. Pont, A. J. van Doorn, A. M. L. Kappers, and J. T. Todd, "The visual light field," Perception **36**(11), 1595–1610 (2007).
7. R. Ramamoorthi, "Modeling Illumination Variation with Spherical Harmonics," in *Face Processing* (Elsevier, 2006), pp. 385–424.
8. L. Xia, S. Pont, and I. Heynderickx, "Light diffuseness metric Part 1: Theory," Light. Res. Technol. **49**(4), 411–427 (2017).
9. A. A. Mury, S. C. Pont, and J. J. Koenderink, "Structure of light fields in natural scenes," Appl. Opt. **48**(28), 5386–5395 (2009).
10. A. A. Mury, S. C. Pont, and J. J. Koenderink, "Representing the light field in finite three-dimensional spaces from sparse discrete samples," Appl. Opt. **48**(3), 450–457 (2009).
11. A. A. Mury, S. C. Pont, and J. J. Koenderink, "Light field constancy within natural scenes," Appl. Opt. **46**(29), 7308–7316 (2007).
12. T. Kartashova, D. Sekulovski, H. de Ridder, S. F. te Pas, and S. C. Pont, "The global structure of the visual light field and its relation to the physical light field," J. Vis. **16**(10), 9 (2016).
13. S. C. Pont, "Light: Toward a transdisciplinary science of appearance and atmosphere," Annu. Rev. Vis. Sci. **5**(1), 503–527 (2019).
14. C. Yu, M. Wijntjes, E. Eisemann, and S. Pont, "Effects of inter-reflections on the correlated colour temperature and colour rendition of the light field," Light. Res. Technol. **5**, 147715352211269 (2022).
15. S. C. Pont, "Ecological optics of natural materials and light fields," in *Human Vision and Electronic Imaging XIV*, B. E. Rogowitz and T. N. Pappas, eds. (SPIE, 2009), 7240, p. 724009.
16. L. Xia, S. C. Pont, and I. Heynderick, "Separate and simultaneous adjustment of light qualities in a real scene," i-Perception **8**(1), 204166951668608 (2017).
17. L. Xia, S. C. Pont, and I. Heynderickx, "Effects of scene content and layout on the perceived light direction in 3D spaces," J. Vis. **16**(10), 14 (2016).
18. C. Cuttle, "Lighting patterns and the flow of light," Light. Res. Technol. **3**(3), 171–189 (1971).
19. F. Zhang, H. de Ridder, P. Barla, and S. Pont, "A systematic approach to testing and predicting light-material interactions," J. Vis. **19**(4), 11 (2019).
20. D.-E. Nilsson and J. Smolka, "Quantifying biologically essential aspects of environmental light," J. R. Soc. Interface **18**(177), 20210184 (2021).
21. T. Morimoto, S. Kishigami, J. M. M. Linhares, S. M. C. Nascimento, and H. E. Smithson, "Hyperspectral environmental illumination maps: characterizing directional spectral variation in natural environments," Opt. Express **27**(22), 32277 (2019).
22. L. Shiwen, L. Steel, C. A. Dahlsjö, S. N. Peirson, A. Shenkin, T. Morimoto, H. E. Smithson, and M. Spitschan, "Hyperspectral characterization of natural illumination in woodland and forest environments," in *Novel Optical Systems, Methods, and Applications XXIV*, C. F. Hahlweg and J. R. Mulley, eds. (SPIE, 2021), p. 7.
23. A. I. Ruppertsberg and M. Bloj, "Creating physically accurate visual stimuli for free: Spectral rendering with RADIANCE," Behav. Res. Methods **40**(1), 304–308 (2008).
24. J. Koenderink, A. van Doorn, and K. Gegenfurtner, "RGB colors and ecological optics," Front. Comput. Sci. **3**, 14 (2021).
25. C. Cuttle, "Cubic illumination," Light. Res. Technol. **29**(1), 1–14 (1997).
26. R. Ramamoorthi and P. Hanrahan, "An efficient representation for irradiance environment maps," in Proceedings of the 28th Annual Conference on Computer Graphics and Interactive Techniques - SIGGRAPH '01 (ACM Press, 2001), pp. 497–500.
27. L. Xia, S. Pont, and I. Heynderickx, "Light diffuseness metric, Part 2: Describing, measuring and visualizing the light flow and diffuseness in three-dimensional spaces," Light. Res. Technol. **49**(4), 428–445 (2017).
28. L. Xia, T. Tian, R. Xu, T. Zhang, and X. Liu, "Measuring low-order photometric parameters of light fields: methods exploration and simulations," IEEE Access **8**, 97408–97417 (2020).

Optics EXPRESS

29. R. Basri and D. Jacobs, "Lambertian reflectance and linear subspaces," in Proceedings Eighth IEEE International Conference on Computer Vision. ICCV 2001 (IEEE Comput. Soc, 2001), 2, pp. 383–390.
30. W. J. Adams, J. H. Elder, E. W. Graf, J. Leyland, A. J. Lugtigheid, and A. Muryy, "The Southampton-York Natural Scenes (SYNS) dataset: Statistics of surface attitude," Sci. Rep. **6**(1), 35805 (2016).
31. Y. Morgenstern, W. S. Geisler, and R. F. Murray, "Human vision is attuned to the diffuseness of natural light," J. Vis. **14**(9), 15 (2014).
32. T. J. Bihl, J. A. Martin, K. C. Gross, and K. W. Bauer, "Data and Feature Fusion Approaches for Anomaly Detection in Polarimetric Hyperspectral Imagery," in NAECON 2021 - IEEE National Aerospace and Electronics Conference (IEEE, 2021), pp. 157–163.
33. A. F. H. Goetz, G. Vane, J. E. Solomon, and B. N. Rock, "Imaging spectrometry for Earth remote sensing," Science **228**(4704), 1147–1153 (1985).
34. C. Fischer and I. Kakoulli, "Multispectral and hyperspectral imaging technologies in conservation: current research and potential applications," Stud. Conserv. **51**(sup1), 3–16 (2006).
35. J. Hernández-Andrés, J. Romero, J. L. Nieves, and R. L. Lee, "Color and spectral analysis of daylight in southern Europe," J. Opt. Soc. Am. A **18**(6), 1325 (2001).
36. D. B. Judd, D. L. MacAdam, G. Wyszecki, H. W. Budde, H. R. Condit, S. T. Henderson, and J. L. Simonds, "Spectral distribution of typical daylight as a function of correlated color temperature," J. Opt. Soc. Am. **54**(8), 1031 (1964).
37. M. Spitschan, G. K. Aguirre, D. H. Brainard, and A. M. Sweeney, "Variation of outdoor illumination as a function of solar elevation and light pollution," Sci. Rep. **6**(1), 26756 (2016).
38. C. Yu, E. Eisemann, and S. Pont, "Effects of inter-reflections on the chromatic structure of the light field," *Light. Res. Technol.*, 147715352110582 (2022).
39. C. Cuttle, *Lighting by Design* (Routledge, 2008).
40. E. . Carter, J. . Schanda, R. Hirschler, S. Jost, M. . Luo, M. Melgosa, Y. Ohno, M. . Pointer, D. . Rich, F. Viénot, L. Whitehead, and J. . Wold, *Colorimetry*, 4th Edition. CIE 015:2018 (CIE Central Bureau, 2018).
41. A. Stockman and L. T. Sharpe, "The spectral sensitivities of the middle- and long-wavelength-sensitive cones derived from measurements in observers of known genotype," Vision Res. **40**(13), 1711–1737 (2000).
42. T. Kartashova, H. de Ridder, S. F. te Pas, and S. C. Pont, "Visual light zones," i-Perception **9**(3), 1–20 (2018).
43. M. Madsen, "Light-zone(s): as concept and tool," Enq. ARCC J. Archit. Res. **4**(1), 50 (2007).
44. C. Yu, "Spectral dataset of natural light fields measured in the Netherlands," Zenodo (2022) https://doi.org/10.5281/zenodo.7328594.
45. S. C. Pont and J. J. Koenderink, "Bidirectional texture contrast function," Int. J. Comput. Vis. **62**(1-2), 17–34 (2005).
46. M. R. Luo, G. Cui, and B. Rigg, "The development of the CIE 2000 colour-difference formula: CIEDE2000," Color Res. Appl. **26**(5), 340–350 (2001).
47. A. Akbarinia and K. R. Gegenfurtner, "Color metamerism and the structure of illuminant space," J. Opt. Soc. Am. A **35**(4), B231 (2018).
48. R. L. Lee and J. Hernández-Andrés, "Colors of the daytime overcast sky," Appl. Opt. **44**(27), 5712 (2005).
49. S. M. C. Nascimento, K. Amano, and D. H. Foster, "Spatial distributions of local illumination color in natural scenes," Vision Res. **120**, 39–44 (2016).
50. C. Yu and S. Pont, "Quantifying natural light for lighting and display design," Dig. Tech. Pap. - Soc. Inf. Disp. Int. Symp. **52**(S2), 99–103 (2021).
51. D. H. Foster, K. Amano, and S. M. C. Nascimento, "Time-lapse ratios of cone excitations in natural scenes," Vision Res. **120**, 45–60 (2016).
52. R. L. Lee Jr., W. Meyer, and G. Hoeppe, "Atmospheric ozone and colors of the Antarctic twilight sky," Appl. Opt. **50**(28), F162 (2011).
53. S. Hillaire, "A Scalable and Production Ready Sky and Atmosphere Rendering Technique," Comput. Graph. Forum **39**(4), 13–22 (2020).
54. J. E. Hansen and L. D. Travis, "Light scattering in planetary atmospheres," Space Sci. Rev. **16**(4), 527–610 (1974).
55. P. Minnis, S. Mayor, W. L. Smith, and D. F. Young, "Asymmetry in the diurnal variation of surface albedo," IEEE Trans. Geosci. Remote Sens. **35**(4), 879–890 (1997).
56. O. Pechony, C. Price, and A. P. Nickolaenko, "Relative importance of the day-night asymmetry in schumann resonance amplitude records," Radio Sci. **42**(2), RS2S06 (2007).
57. S. Rickel and A. Genin, "Twilight transitions in coral reef fish: the input of light-induced changes in foraging behaviour," Anim. Behav. **70**(1), 133–144 (2005).
58. D. H. Deutsch, "A mechanism for molecular asymmetry," J. Mol. Evol. **33**(4), 295–296 (1991).